Energy & Environmental Science

PAPER

View Article Online
View Journal | View Issue

Cite this: *Energy Environ. Sci.*, 2016, **9**, 1752

Grain boundary dominated ion migration in polycrystalline organic–inorganic halide perovskite films†

Yuchuan Shao,‡[a] Yanjun Fang,‡[a] Tao Li,‡[b] Qi Wang,‡[a] Qingfeng Dong,[a] Yehao Deng,[a] Yongbo Yuan,[a] Haotong Wei,[a] Meiyu Wang,[a] Alexei Gruverman,[b] Jeffery Shield[a] and Jinsong Huang*[a]

Received 9th February 2016,
Accepted 21st March 2016

DOI: 10.1039/c6ee00413j

www.rsc.org/ees

The efficiency of perovskite solar cells is approaching that of single-crystalline silicon solar cells despite the presence of a large grain boundary (GB) area in the polycrystalline thin films. Here, by using a combination of nanoscopic and macroscopic level measurements, we show that ion migration in polycrystalline perovskites dominates through GBs. Atomic force microscopy measurements reveal much stronger hysteresis both for photocurrent and dark-current at the GBs than on the grain interiors, which can be explained by faster ion migration at the GBs. The dramatically enhanced ion migration results in the redistribution of ions along the GBs after electric poling, in contrast to the intact grain area. The perovskite single-crystal devices without GBs show negligible current hysteresis and no ion-migration signal. The discovery of dominating ion migration through GBs in perovskites can lead to broad applications in many types of devices including photovoltaics, memristors, and ion batteries.

Broader context

Ion migration in organic–inorganic halide perovskites has attracted intense attention because it may be responsible for many unusual behaviors in perovskite based materials and devices, such as photocurrent hysteresis, photo-induced giant dielectric constants, photo-induced phase separation and the absence of transistor behavior at room temperature. Nevertheless, the understanding of ion migration in perovskites is still limited. One fundamental question to be answered is what is the dominating ion migrating channel? Here, by conducting a combination of nanoscopic and macroscopic level measurements, we revealed a much faster ion migration at grain boundaries than that in the grains and showed that the grain boundary ion migration dominated the hysteresis behavior in perovskite solar cells. Our results provide guidance in achieving hysteresis-free perovskite solar cells, and pave the way for the design of many other perovskite-based electronic devices, such as memristors and ion batteries. In addition, our results explain some discrepancies between calculation results and experimental observations on what type of ions diffuse in hybrid perovskites. This points out a direction that future computation needs to consider: grain boundary and surface diffusion.

Introduction

Organometal trihalide perovskites are emerging as very promising photovoltaic materials. Only five years of research has enabled the power conversion efficiency (PCE) of perovskite solar cells to quickly rise from 3.8% to certified 21.0%, rivaling that of single crystal silicon solar cells.[1–14] Recently, a PCE of ~15% was demonstrated in perovskite solar cells with an aperture area larger than one square centimeter.[15] Unlike many types of polycrystalline solar cells based on silicon,[16] cadmium telluride (CdTe),[17] copper indium gallium (di)selenide (CIGS)[18] *etc.* that suffer energy loss due to the carrier recombination processes at GBs, the GBs in the organometal trihalide perovskite polycrystalline films have been shown to be much more benign in this regard,[19,20] which contributes to the very high PCE of polycrystalline perovskite solar cells even though faster charge recombination at GBs than on grains was also recorded.[21] Among all the intriguing properties of perovskites, ion migration has drawn much attention due to its correlation with the unique photocurrent hysteresis behavior,[22–26] and due to the unusual defect physics, *i.e.*, the absence of deep-trap states.[27] Present studies consistently support that the accumulated ions in the polycrystalline perovskite layer near the ion blocking

[a] *Department of Mechanical and Materials Engineering, University of Nebraska-Lincoln, Lincoln, Nebraska 68588, USA. E-mail: jhuang2@unl.edu*
[b] *Department of Physics and Astronomy, University of Nebraska-Lincoln, Lincoln, Nebraska 68588, USA*

† Electronic supplementary information (ESI) available. See DOI: 10.1039/c6ee00413j

‡ These authors contributed equally to this work.

interface as a result of ion migration would induce a larger degree of p- and n-doping, which screens the applied voltage, changes the charge collection efficiency and results in the current hysteresis.[22–25] In addition, ion migration has been proposed to be responsible for many unusual behaviors in perovskites such as photoinduced giant dielectric constants,[28] the absence of transistor behavior at room temperature[29] and photo-induced phase separation.[30] Nevertheless, the understanding of ion migration in polycrystalline perovskite films is very limited. One most fundamental issue to be addressed is what is (are) the ion migrating channel(s)?

Ion migration in polycrystalline films can occur through the bulk of the grains *via* point defects or through extended defects such as GBs. The ion migration rate (r_m) in a solid material is determined by the activation energy (E_A) for ion hopping to be $r_m \propto \exp\left(-\frac{E_A}{k_B T}\right)$, where k_B and T are the Boltzmann constant and temperature, respectively. E_A is influenced by many factors, such as the size and charge of the ions, the hopping distance, and the material crystal structure. Similar to the diffusion process, ion-migration under an electric field needs the aid of defects. In general, ion migration is more pronounced at the GBs, because the activation energy at GBs is much smaller with the extended defects.[31] However, this expectation is not always true. In some mixed ionic-electronic materials such as $Ce_{0.8}Gd_{0.2}O_{2-\delta}$, the ionic migration through GBs can be suppressed due to the dopant segregation at GBs.[32] Whether ion migration predominately goes through the grain bulk or GBs in perovskite polycrystalline films remains unknown for two reasons. First, theoretical work predicted a huge Schottky defect density of 0.4% at room temperature,[33] which boosts bulk ion migration. In addition, since nowadays most perovskite thin films are fabricated *via* the low-temperature solution process, a large density of defects inevitably exists in the bulk of perovskite grains. Although these defects would not generate deep traps because of the unusual defect physics of perovskites, they could still assist the ion "hopping" in increasing the bulk ion migration rate. Second, the ion migration flux is determined by the product of the ion migration rate and the ion migration channel area, while the cross-section area for bulk ion migration is much larger than that for GB ion migration.

In this work, we report that GB ion migration is not only much faster than bulk ion migration, but also dominates the migration process in the polycrystalline thin films formed using the low temperature solution method, which results in the unique photocurrent hysteresis behavior of perovskite solar cells.

Results and discussion

To examine the ion transportation of polycrystalline perovskite thin films, we measured the ion migration associated local

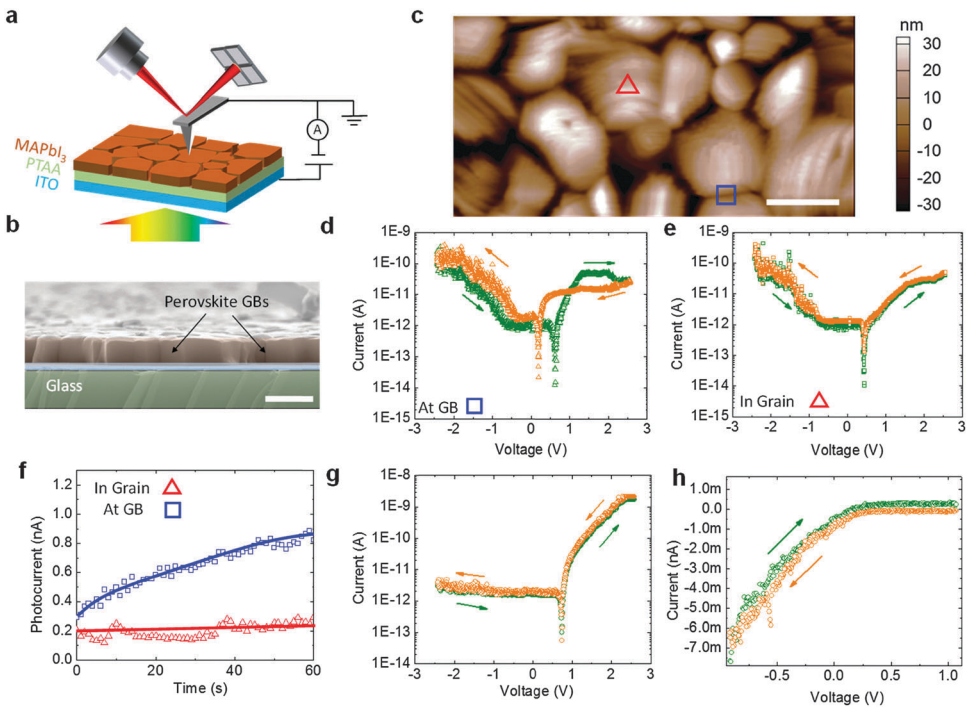

Fig. 1 Local currents measured by c-AFM. (a) c-AFM measurement setup. (b) Cross-section SEM image of the perovskite thin film used in c-AFM measurement. The scale bar is 1 μm. (c) Topography AFM image of the perovskite thin film. The locations where the c-AFM tip measured the grain and GB current are labeled with a red triangle and a blue square, respectively. The scale bar is 1 μm. (d and e) Local dark current measured at the GB (d) and on the grain (e), respectively. (f) Steady-state photocurrent (absolute value) measured under short circuit conditions at the grain (red triangle) and at the GB (blue square), respectively. Red and blue solid lines are guidelines. (g and h) Local dark-current (g) and photocurrent (h) measured at the GB in perovskite thin films covered by PCBM.

current hysteresis at GBs and on grains using conductive atomic force microscopy (c-AFM). A larger current hysteresis would indicate a quicker ion migration locally during the current scanning process. Fig. 1a illustrates the c-AFM setup for both the dark-current and photocurrent measurements. For the local photocurrent measurements, the samples were illuminated from the indium tin oxide (ITO) side using a white light source with an intensity of 20 mW cm^{-2}. The continuous $CH_3NH_3PbI_3$ perovskite thin films used in this study were fabricated through interdiffusion of lead iodide (PbI_2) and methyl ammonium iodide (CH_3NH_3I, CH_3NH_3 = MA) stacking layers.[34] Solvent annealing was applied to grow large and highly crystalline grains. Photovoltaic devices based on such high-quality perovskite polycrystalline thin films with a device structure of ITO/poly[bis(4-phenyl)(2,4,6-trimethylphenyl)amine] (PTAA)/perovskite/phenyl-C61-butyric acid methyl ester (PCBM)/C_{60}/2,9-dimethyl-4,7-diphenyl-1,10-phenanthroline (BCP)/aluminum (Al) yield a high power conversion efficiency above 19.0%.[35,36] The cross-section scanning electron microscopy (SEM) image, shown in Fig. 1b, reveals two important features of these films that enable the study of ion migration along GBs by c-AFM: first, the lateral size of grains is much larger than the film thickness; second, most GBs are aligned perpendicular to the ITO substrate. Therefore the charge transport or ion migration inside grains would not encounter GBs, which underpins our local current hysteresis measurement.

The local dark-currents of the bare perovskite films were measured by positioning conductive AFM tips at the specific locations determined from the AFM topographic image (Fig. 1c) and sweeping the tip bias in the range between 2.5 V and −2.5 V at a rate of 0.14 V s^{-1}. The c-AFM measurements did not cause damage to the perovskite thin film surfaces, as shown in Fig. S1 (ESI†). Here, we refer the currents measured at the GB area and at a point at least 300 nm away from the GBs as "GB current" and "grain current", respectively. As shown in Fig. 1d and e, the GB dark-current shows clear hysteresis, similar to the macroscopic dark-current measured in the devices with the ITO/PTAA/perovskite/Au structure. In sharp contrast, the measured grain dark-current shows negligible hysteresis. It shows that the dark-current was not subject to the hysteresis if the c-AFM tip was placed about ~100 nm away from the GB for a 500 nm-thick perovskite film (Fig. S2, ESI†), confirming the effectiveness of the study of GB and bulk ion migration. Applying different loading forces on the c-AFM tip changed the magnitude of the dark-current due to the changed tip/sample contact area, but it did not change the conclusion of a stronger current hysteresis at GBs (Fig. S3, ESI†). Statistical dark-current results measured at 50 points of the GBs and grain interiors are summarized in Fig. S4 (ESI†), demonstrating a good reproducibility of the results. This observation suggests that the ions more readily migrate at GBs. Opposite to the general intuition, we previously showed that photovoltage driven ion-migration actually increases the perovskite solar cell efficiency,[37] which might explain the measured long lifetime of perovskite solar cells despite the occurrence of ion migration in these cells. Here, we also confirmed this at the nanoscopic level. By placing the c-AFM tip on GBs, a gradual increase of short circuit current was observed after the device was exposed to illumination while the short circuit current measured atop of grains almost remained unchanged (Fig. 1f). Previously, it has been confirmed that PCBM could eliminate the photocurrent hysteresis by diffusing into the GB during long time thermal annealing,[35] which passivated the deep charge traps by interaction with defects such as I–Pb antisite.[11] The ion diffusion is expected to be suppressed as well by filling the relatively open grain boundaries with the non-mobile fullerene-balls which also interact with defects at GBs.[11] Here, the c-AFM results obtained for the OTP thin films covered by PCBM also confirm, at the nanoscopic level, that both the dark-current and photocurrent hysteresis at GBs could be suppressed due to the presence of PCBM, as shown in Fig. 1g and h.

The local photocurrents also exhibit a similar hysteresis behavior, which is strong at GBs, and almost disappears on the grains. It is noted that there is variation in the magnitude of

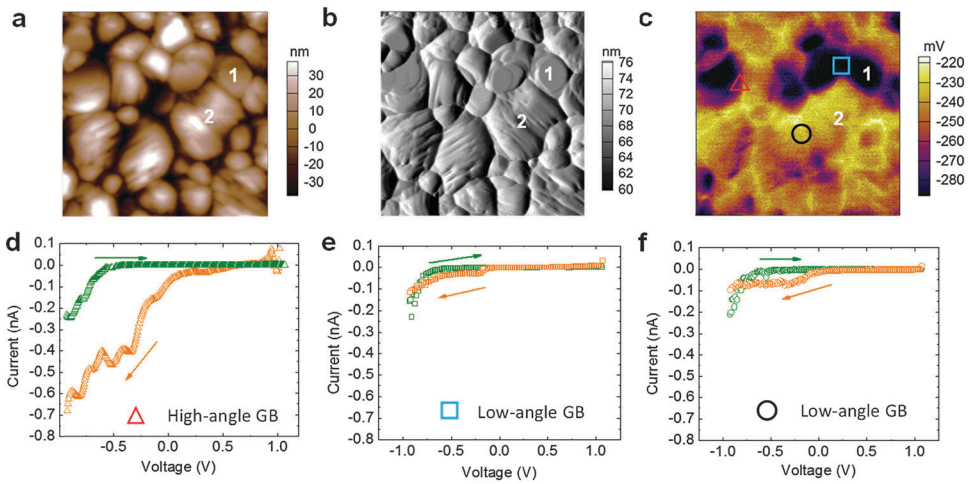

Fig. 2 Grain boundary morphology dependent current measured by c-AFM. Height (a) and amplitude (b) images of the same area of a perovskite thin film; (c) KPFM image showing the locations where the c-AFM tip measured the photocurrents. (d–f) Photocurrents measured at the location labeled in (c) with forward and reverse scanning at a scan rate of 0.14 V s^{-1}.

photocurrent hysteresis at different GBs, suggesting a correlation of photocurrent hysteresis with GB morphology. The topography of the perovskite polycrystalline films is featured with two different types of grains: one shows a smooth surface while the other has a layered texture as shown by the AFM topography in Fig. 2a and b and the SEM image in Fig. S5 (ESI†). Transmission electron microscopy (TEM) measurements revealed that the two types of grains have different crystallographic orientations (Fig. S6, ESI†). The difference between these two types of grains is more distinct in the surface potential maps (Fig. 2c), which were obtained by Kelvin-probe-force microscopy (KPFM) measurements. Grain #1 with a smooth surface has a larger surface work function than that of grain #2 with a textured surface. Therefore, we can infer the angle between the GBs from their surface potential difference. The GBs between grains with a large difference of surface potential should have a larger angle than those between grains with small or no difference of surface potential. As shown in Fig. 2d–f, the local photocurrents show stronger hysteresis at large-angle GBs, but relatively much smaller hysteresis at low-angle GBs. These results are consistent with a general assumption that the large-angle GBs have more open structures and less lattice strain.[38]

The faster ion migration at GBs was also studied at the microscopic and macroscopic levels by changing the perovskite grain or crystallite size. A larger grain size reduces the GB area, and thus reduces current hysteresis in the devices, which is verified in this work. Here a combination of thermal annealing and wetting surface was applied to obtain small size grains (~300 nm),[34] and a combination of solvent annealing and non-wetting surface was applied to obtain larger size grains (1–5 μm),[36] and we used single crystals with lateral size of several millimeters as the extreme case of very large grains. High quality $MAPbBr_3$ single crystals grown using the anti-solvent method were used. It was confirmed by the polarized light microscopy image that these $MAPbBr_3$ single crystals are free of GBs due to the optimized growth method.[39] As shown in Fig. 3a–c, the dark-current hysteresis reduces with the increase of the grain size. No current hysteresis was observed in the $MAPbBr_3$ single-crystal device regardless of the scanning rates (Fig. S7, ESI†), supporting the role of GB in inducing the current hysteresis.

Faster ion migration in films with smaller grains results in a larger contribution of ionic conductivity to the total conductivity, which is confirmed by galvanostatic direct current (DC) measurements.[26] In these measurements, the perovskite single crystals and thin films were sandwiched between ion-blocking electrodes and placed in a N_2 filled glovebox to avoid any oxidation and hydrolysis. A small DC current (2 nA and 2 μA for single crystals and thin film devices, respectively) was applied to the devices in the dark, when the change in voltage across the devices *versus* time was recorded. The initial conductivity includes both the electronic and ionic conductivities, while the steady conductivity should be ascribed only to the electronic conductivity, because blocking of ions by the electrodes results in an internal ion gradient which consequently impedes further ion migration.[26] As shown in Fig. 3d, the voltage of the single crystal device was

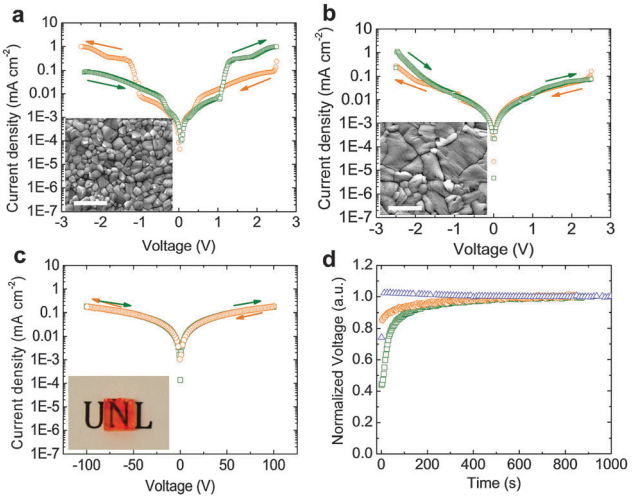

Fig. 3 Grain size dependent ion migration in perovskite materials measured at the macroscopic level. (a–c) Dark-current of (a) thermally-annealed thin-film devices, (b) solvent-annealed thin-film devices, and (c) single crystal devices. The insets in (a–c) show typical grains with size increased from several hundred nanometers to several millimeters. The scale bar of the SEM image is 2 μm. (d) Galvanostatic direct current (DC) of the thermally-annealed thin-film devices (green square), solvent-annealed thin-film devices (orange circle) and the single crystal devices (blue triangle).

kept almost constant through a 900 s scanning process after a short stabilization process of about five seconds, in contrast to a gradually increased voltage in the first two minutes of the polycrystalline perovskite films. This confirms the negligible conductivity contribution from the ion migration in the single-crystal devices, which agrees well with the hysteresis-free current in the single crystal devices.

The faster ion migration at GBs has been directly observed by a very different element redistribution along the GBs compared to the grain area after electrical poling. To get a better view of the morphology and composition change along individual GBs after poling, polycrystalline perovskite thin films with a large grain size of several hundred micrometers were adopted to clearly observe the morphology and composition change along one individual GB after poling. These large grain size perovskite films were fabricated using the doctor-blade method,[40] but a much lower blading velocity was applied here in order to increase the grain size. A lateral device structure was used here, consisting of two gold electrodes thermally evaporated on top of the film with a spacing of 100 μm, and a 20 nm thick PCBM layer was spun on top of the device to encapsulate the films and to minimize the surface ion migration. The image (Fig. 4a) of the as-fabricated film clearly shows a GB perpendicular to the two electrode bars and the distribution of composition is uniform. After a moderate poling of 0.5 V μm^{-1} was applied for ~120 s at 330 K, bumps and pin-holes appear on the film (Fig. 4b), in a way similar to that observed in polycrystalline thin films after poling,[23] where these changes primarily occurred at the affinity of electrodes and along the GBs. By increasing the poling voltage to 1.0 V μm^{-1} for a longer poling time of ~300 s, a drastic morphology change was observed along the whole GB throughout the channel (Fig. 4c). The changed morphology close to the electrode can be explained

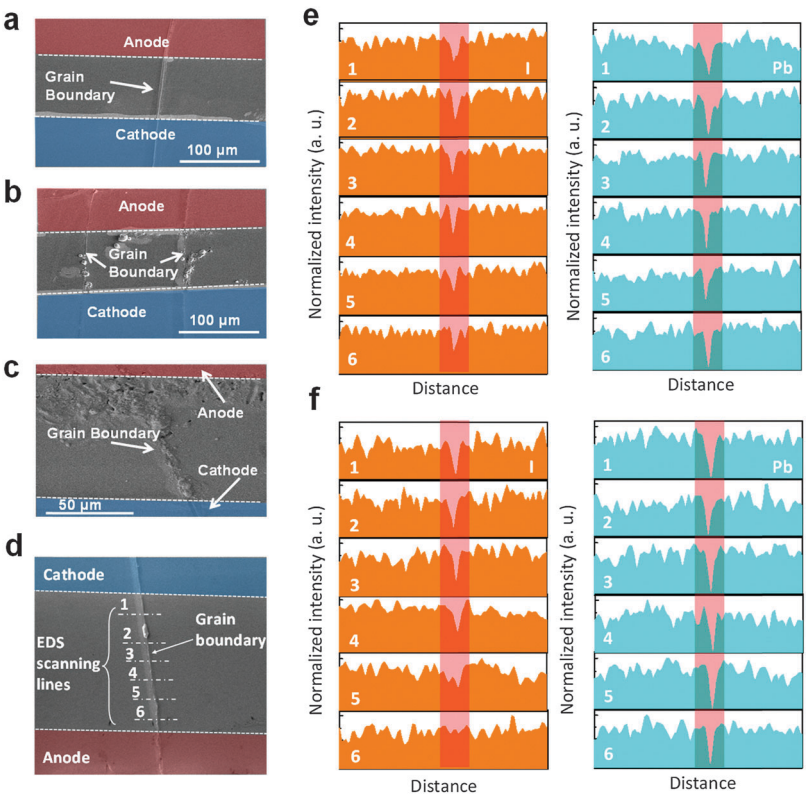

Fig. 4 Element redistribution after electric poling at the GB observed by SEM and EDS. (a) SEM image of an as-grown large-grain $MAPbI_3$ polycrystalline thin film with GB lying perpendicular to the two Au electrodes. (b) SEM image of a large grain perovskite thin film after poling under a bias of 50 V for 120 s, showing that the morphology change primarily occurred near the GB and electrodes. (c) SEM image of a large grain $MAPbI_3$ thin film after poling under a bias of 100 V for 300 s, demonstrating drastic morphology change along the whole GB. (d) SEM image of another as-grown large-grain $MAPbI_3$ polycrystalline thin film with the GB lying perpendicular to the two Au electrodes. The white dash dotted lines represent the EDS scanning lines. (e) EDS line scanning of iodine (orange) and lead element (blue) before poling. Red rectangles indicate the grain boundary area. The number of panels matches the scanning lines in (d). (f) EDS line scanning of iodine (orange) and lead (blue) element after poling.

by the electrochemical reaction of perovskites in the presence of Au catalysts,[41] while the GB morphology change most likely comes from the ion migration along the GB. The intact morphology of the grain areas away from the GB indicates that the ion migration is much faster along the GBs.

To confirm that the ion-migration caused macroscopic element redistribution after poling, energy-dispersive X-ray spectroscopy (EDS) line scanning was carried out. Both iodine and lead elements were traced to detect their ion migration, since they have a large atomic number and can be much easier than MA^+ to be detected by EDS. The white dash dotted lines in Fig. 4d represent the EDS scanning lines. As shown in Fig. 4e, before poling, the signal intensities of both lead and iodine elements at the GBs were lower than that in grains as less perovskites exist at GBs. After a moderate poling of 0.5 V μm^{-1} was applied for ~120 s at 330 K, no obvious change in the lead element distribution was observed (Fig. 4f). In sharp contrast, a clear iodine concentration gradient at the GB increasing from the cathode to the anode side appeared after poling, while the iodine concentration in the grain interior remained unchanged. These results provide conclusive evidence that the ion migration is mainly dominated at the GB region in polycrystalline perovskite thin films.

Finally, we studied the impact of fast ion migration along the GBs on the properties and performance of different electronic devices including photovoltaics and memristors. Memristors are one kind of non-volatile memory devices with the reproducible gradual resistance tuning function. The memristors could be used to mimic the biological synapse and to realize the neuromorphic computers. For photovoltaic devices, it was found that the ion migration enhanced the performance of the devices with a small grain size of ~300 nm (Fig. 5a). The light poling effect drives the ion migration to form a more favorable p–i–n structure, which enhances the charge collection efficiency.[37] The device efficiency gradually increased from 14.8% to 16.7% under one sun illumination for 300 seconds. The results also well explain the observed higher charge collection efficiency at GBs by several groups.[19,20] However, the stabilized PCE of the device with small size grains is still lower than that of the device with large grains (~1 μm), whose PCE is stabilized at 19.0% immediately upon illumination. The different stabilized PCEs of these two types of devices indicate that the GBs in organic–inorganic halide perovskite materials overall are still detrimental in causing a quicker non-radiative charge recombination,[36] while light-induced ion migration narrowed down the difference. On the other hand, the quicker ion migration along GBs clearly

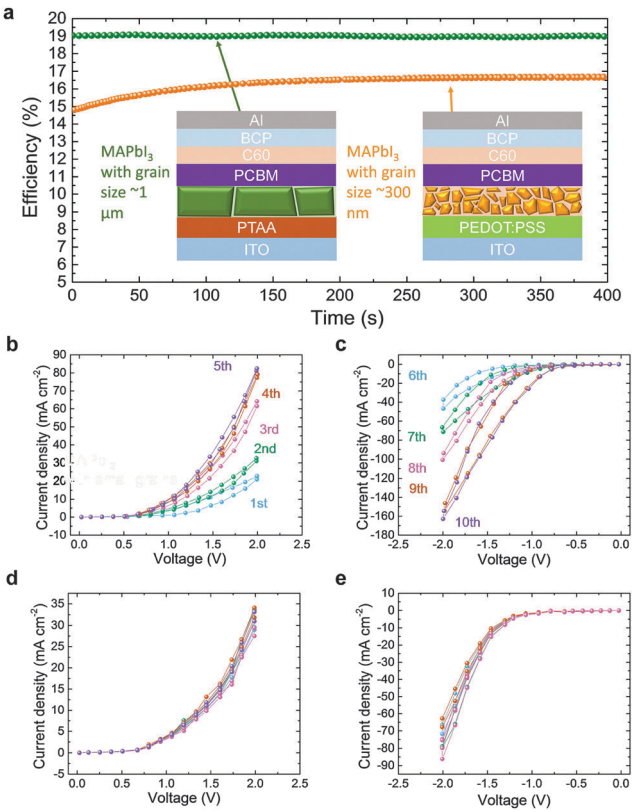

Fig. 5 The effect of GB density on solar cell and memristor device performance. (a) Steady-state efficiency measurement of the perovskite solar cells with different grain sizes. (b and c) Memristive characteristics of the device with large grains under the positive and negative bias scanning. The scanning rate is 0.14 V s^{-1}. (d and e) No memristive characteristics in the devices with small grains under the positive and negative bias scanning. The scanning rate is 0.14 V s^{-1}.

plays beneficial roles in the perovskite memristors, which rely on ion migration to form a switchable p–i–n structure. To demonstrate this, devices with the same structure as ITO/PEDOT:PSS/$MAPbI_3$/Au but different grain sizes were fabricated with and without using solvent annealing. The devices made of small perovskite grains (~300 nm) showed obvious memristive behavior at a scanning rate of 0.1 V s^{-1} (Fig. 5b and c): when consecutive negative bias (0 to −2.0 V) sweeps were applied on the device, the dark current density continuously increased, which indicates that the negative bias scanning gradually switches the device to n–i–p polarity, because negative bias works as forward bias for the n–i–p polarity. Similarly, when consecutive positive (0 to 2.0 V) sweeps were applied on the devices, the dark current density also continuously increased. In sharp contrast, the devices made of large perovskite grains (~1 μm) showed no memristive behavior (Fig. 5d and e). The results demonstrated the beneficial role of GBs in memristors by providing the necessary fast ion migration channels.

In summary, a faster ion migration at GBs in comparison to that in grain interiors was discovered by a combination of nanoscopic and macroscopic level electrical measurements. The results are crucial for the understanding of the role of GBs in photovoltaic device performance. In addition, it has been reported that lead halide perovskites could be used in batteries as lithium storage materials, which initially store up to ~330 mAh g^{-1}. The remarkable capacity is competitive with the state-of-the-art anode materials.[42] A faster charging rate would be expected with a larger density of the GB area. Our work also provides guidance in studying what kinds of ions migrate in perovskites at room temperature. Up to now, some theoretical studies have predicted that I^- ions move more readily than MA^+ and Pb^{2+} ions.[33,43,44] However, only the redistribution of MA^+ ions was observed experimentally at room temperature while the migration of I^- ions needs to be realized at increased temperature.[26,41,45] Our results could explain the discrepancy between calculation and experimental results. The previous calculations only consider the ion migrations through the bulk. However, we gave direct evidence that ion migration *via* grain boundaries is much more important than bulk diffusion in real polycrystalline films.

Methods

Perovskite thin film device fabrication

The buffer layer, PTAA film, was prepared by spin-coating 0.5 wt% PTAA solution with 6000 rpm, followed by a thermal annealing process at 110 °C for 10 min. Then, the $MAPbI_3$ films were fabricated using the interdiffusion method. The film fabrication procedures are the same as in previous studies, while the PbI_2 layer on PTAA should be spin-coated from 100 °C pre-heated PbI_2 DMF solution. To fabricate 500 nm thick $MAPbI_3$ films, 650 mg ml^{-1} PbI_2 DMF precursors were used with 75 mg ml^{-1} methylammonium iodide (MAI) 2-propanol precursor solution. The formed $MAPbI_3$ thin films have an average grain size of ~300 nm. For $MAPbI_3$ thin films with an average grain size of ~600 nm, solvent annealing is conducted to increase the grain size as in previous studies.[24] For devices with PCBM layers, PCBM (dissolved in dichlorobenzene (DCB), 2 wt%) was spun on top of the formed perovskite layers. After that, the devices were finished by thermal evaporation of gold (Au, 50 nm). The device working area was 8 mm^2, defined by the overlap of an ITO substrate and an Au electrode.

Sub-millimeter-sized-grain perovskite thin film device fabrication

To grow the large grain perovskite thin film on a glass substrate, we used the slow doctor blade coating method to minimize nucleation and guide the crystal growth. Typically, $MAPbI_3$ precursor solution (90 mg ml^{-1}) is dropped onto the UV-ozone treated glass substrate pre-heated at 140 °C and then the solution is slowly bladed using a glass slide connected to a syringe pump to spread over the glass substrate at a rate of 0.1 mm s^{-1}. Then the as-prepared perovskite film is annealed first at 120 °C for 20 min and then at 100 °C for 1 hour to completely dry the film. Then, 50 nm thick Au was thermally evaporated on the film using a shadow mask as a coplanar electrode. Lastly, 20 nm thick PCBM (in DCB, 2 wt%) was spin-coated on top of the device to encapsulate the surface of the perovskite film.

Conductive atomic force microscopy (c-AFM) and Kelvin probe force microscopy (KPFM)

A commercial AFM system (MFP-3D, Asylum Research, USA) and Pt/Ir coated conductive probes (PPP-EFM, Nanosensors, Switzerland) were used to perform the c-AFM and KPFM measurements. In our KPFM measurement, a two-pass technique was employed. The first pass was used to acquire the topographic height, and then the conductive probe was lifted with respect to the specimen surface with a constant separation, approximately 10 nm here, and scanned to acquire the potential offset between the tip and the sample. An AC bias of 2 V amplitude at the first contact resonance frequency and a DC bias of 1 V were applied to the conductive probe.

Electrical characterization

The dark currents of thermally annealed and solvent annealed perovskite thin film devices were recorded using a Keithley 2400 semiconductor analyzer. The scanning rate is 0.14 V s^{-1}. For galvanostatic direct current (DC) measurements, a constant bias current of 2 μA and 2 nA was applied for thin film devices and single crystal devices, respectively, because of their different thickness. During all electrical characterization, perovskite devices were kept in a N_2 glovebox to protect the samples.

Energy-dispersive X-ray spectroscopy (EDS)

The EDS line scanning was carried out on a FEI Nova NanoSEM 450 instrument equipped with an Oxford X-MAX energy dispersive X-ray spectroscope. The typical electron acceleration voltage for X-ray excitation was 10 kV. The large-grain perovskite lateral device for the EDS measurement was electrically poled in a probe station in a vacuum under different voltage bias and with different poling duration.

Competing financial interests

The authors declare no competing financial interests.

Author contributions

Y. S., Y. F., T. L. and Q. W. contributed to this work equally. J. H. conceived the idea, designed the experiments and supervised the whole project. Y. S. fabricated the thin film devices and conducted their measurements. Y. F. fabricated the single crystal devices and conducted their measurements. T. L. conducted the c-AFM measurements. Q. W. conducted the EDS and TEM measurements. Y. Y. conducted the SEM measurements. Y. D. fabricated the large grain perovskite thin films. H. W. synthesized the $CH_3NH_3Br_3$ single crystals. J. H., A. G., Y. S. and Y. F. wrote the paper.

Acknowledgements

We are grateful for the financial support from the National Science Foundation (DMR-1505535 and DMR-1420645), Department of Energy (DE-EE0006709), and Office of Naval Research (N00014-15-1-2713).

References

1 M. Liu, M. B. Johnston and H. J. Snaith, *Nature*, 2013, **501**, 395–398.
2 H. Zhou, Q. Chen, G. Li, S. Luo, T.-b. Song, H.-S. Duan, Z. Hong, J. You, Y. Liu and Y. Yang, *Science*, 2014, **345**, 542–546.
3 J. Burschka, N. Pellet, S.-J. Moon, R. Humphry-Baker, P. Gao, M. K. Nazeeruddin and M. Grätzel, *Nature*, 2013, **499**, 316–319.
4 M. A. Green, A. Ho-Baillie and H. J. Snaith, *Nat. Photonics*, 2014, **8**, 506–514.
5 M. D. McGehee, *Nat. Mater.*, 2014, **13**, 845–846.
6 Q. Lin, A. Armin, R. C. R. Nagiri, P. L. Burn and P. Meredith, *Nat. Photonics*, 2015, **9**, 106–112.
7 N. J. Jeon, J. H. Noh, W. S. Yang, Y. C. Kim, S. Ryu, J. Seo and S. I. Seok, *Nature*, 2015, **517**, 476–480.
8 D. Shi, V. Adinolfi, R. Comin, M. Yuan, E. Alarousu, A. Buin, Y. Chen, S. Hoogland, A. Rothenberger and K. Katsiev, *Science*, 2015, **347**, 519–522.
9 P. W. Liang, C. Y. Liao, C. C. Chueh, F. Zuo, S. T. Williams, X. K. Xin, J. Lin and A. K. Y. Jen, *Adv. Mater.*, 2014, **26**, 3748–3754.
10 Y. Wu, A. Islam, X. Yang, C. Qin, J. Liu, K. Zhang, W. Peng and L. Han, *Energy Environ. Sci.*, 2014, **7**, 2934–2938.
11 J. Xu, A. Buin, A. H. Ip, W. Li, O. Voznyy, R. Comin, M. Yuan, S. Jeon, Z. Ning and J. J. McDowell, *Nat. Commun.*, 2015, **6**, 7081.
12 H.-S. Kim, C.-R. Lee, J.-H. Im, K.-B. Lee, T. Moehl, A. Marchioro, S.-J. Moon, R. Humphry-Baker, J.-H. Yum and J. E. Moser, *Sci. Rep.*, 2012, **2**, 591.
13 A. Kojima, K. Teshima, Y. Shirai and T. Miyasaka, *J. Am. Chem. Soc.*, 2009, **131**, 6050–6051.
14 NREL, http://www.nrel.gov/ncpv/images/efficiency_chart.jpg, 2016.
15 W. Chen, Y. Wu, Y. Yue, J. Liu, W. Zhang, X. Yang, H. Zhen, E. Bi, I. Ashraful, M. Grätzel and L. Han, *Science*, 2015, **350**, 944–948.
16 T. Distefano and J. J. Cuomo, *Appl. Phys. Lett.*, 1977, **30**, 351–353.
17 J. Britt and C. Ferekides, *Appl. Phys. Lett.*, 1993, **62**, 2851–2852.
18 M. Gloeckler, J. R. Sites and W. K. Metzger, *J. Appl. Phys.*, 2005, **98**, 113704.
19 J. S. Yun, A. Ho-Baillie, S. Huang, S. H. Woo, Y. Heo, J. Seidel, F. Huang, Y.-B. Cheng and M. A. Green, *J. Phys. Chem. Lett.*, 2015, **6**, 875–880.
20 B. Yang, O. Dyck, J. Poplawsky, J. Keum, A. Puretzky, S. Das, I. Ivanov, C. Rouleau, G. Duscher and D. Geohegan, *J. Am. Chem. Soc.*, 2015, **137**, 9210–9213.
21 D. W. de Quilettes, S. M. Vorpahl, S. D. Stranks, H. Nagaoka, G. E. Eperon, M. E. Ziffer, H. J. Snaith and D. S. Ginger, *Science*, 2015, **348**, 683–686.
22 H. J. Snaith, A. Abate, J. M. Ball, G. E. Eperon, T. Leijtens, N. K. Noel, S. D. Stranks, J. T.-W. Wang, K. Wojciechowski and W. Zhang, *J. Phys. Chem. Lett.*, 2014, **5**, 1511–1515.

23 Z. Xiao, Y. Yuan, Y. Shao, Q. Wang, Q. Dong, C. Bi, P. Sharma, A. Gruverman and J. Huang, *Nat. Mater.*, 2015, **14**, 193–198.
24 W. Tress, N. Marinova, T. Moehl, S. Zakeeruddin, M. K. Nazeeruddin and M. Grätzel, *Energy Environ. Sci.*, 2015, **8**, 995–1004.
25 E. Unger, E. Hoke, C. Bailie, W. Nguyen, A. Bowring, T. Heumüller, M. Christoforo and M. McGehee, *Energy Environ. Sci.*, 2014, **7**, 3690–3698.
26 T. Y. Yang, G. Gregori, N. Pellet, M. Grätzel and J. Maier, *Angew. Chem.*, 2015, **127**, 8016–8021.
27 W.-J. Yin, T. Shi and Y. Yan, *Appl. Phys. Lett.*, 2014, **104**, 063903.
28 E. J. Juarez-Perez, R. S. Sanchez, L. Badia, G. Garcia-Belmonte, Y. S. Kang, I. Mora-Sero and J. Bisquert, *J. Phys. Chem. Lett.*, 2014, **5**, 2390–2394.
29 X. Y. Chin, D. Cortecchia, J. Yin, A. Bruno and C. Soci, *Nat. Commun.*, 2015, **6**, 7383.
30 E. T. Hoke, D. J. Slotcavage, E. R. Dohner, A. R. Bowring, H. I. Karunadasa and M. D. McGehee, *Chem. Sci.*, 2015, **6**, 613–617.
31 H. Mehrer, *Diffusion in Solids: Fundamentals, Methods, Materials, Diffusion-Controlled Processes*, Springer, Berlin, Heidelberg, 2007.
32 Y. Lin, S. Fang, D. Su, K. S. Brinkman and F. Chen, *Nat. Commun.*, 2015, **6**, 6824.
33 C. Eames, J. M. Frost, P. R. Barnes, B. C. O'regan, A. Walsh and M. S. Islam, *Nat. Commun.*, 2015, **6**, 7497.
34 Z. Xiao, C. Bi, Y. Shao, Q. Dong, Q. Wang, Y. Yuan, C. Wang, Y. Gao and J. Huang, *Energy Environ. Sci.*, 2014, **7**, 2619–2623.
35 Y. Shao, Z. Xiao, C. Bi, Y. Yuan and J. Huang, *Nat. Commun.*, 2014, **5**, 5784.
36 C. Bi, Q. Wang, Y. Shao, Y. Yuan, Z. Xiao and J. Huang, *Nat. Commun.*, 2015, **6**, 7747.
37 Y. Deng, Z. Xiao and J. Huang, *Adv. Energy Mater.*, 2015, **5**, 1500721.
38 P. Lejcek, *Grain Boundary Segregation in Metals*, Springer, 2010.
39 H. Wei, Y. Fang, P. Mulligan, W. Chuirazzi, H. Fang, C. Wang, B. Ecker, Y. Gao, M. A. Loi, L. Cao and J. Huang, *Nat. Photonics*, 2016, DOI: 10.1038/nphoton.2016.41.
40 Y. Deng, E. Peng, Y. Shao, Z. Xiao, Q. Dong and J. Huang, *Energy Environ. Sci.*, 2015, **8**, 1544–1550.
41 T. Leijtens, E. T. Hoke, G. Grancini, D. J. Slotcavage, G. E. Eperon, J. M. Ball, M. De Bastiani, A. R. Bowring, N. Martino and K. Wojciechowski, *Adv. Energy Mater.*, 2015, **5**, 1500962.
42 H.-R. Xia, W.-T. Sun and L.-M. Peng, *Chem. Commun.*, 2015, **51**, 13787–13790.
43 J. M. Azpiroz, E. Mosconi, J. Bisquert and F. De Angelis, *Energy Environ. Sci.*, 2015, **8**, 2118–2127.
44 J. Haruyama, K. Sodeyama, L. Han and Y. Tateyama, *J. Am. Chem. Soc.*, 2015, **137**, 10048–10051.
45 Y. Yuan, Q. Wang, Y. Shao, H. Lu, T. Li, A. Gruverman and J. Huang, *Adv. Energy Mater.*, 2015, **6**, 1501803.